

# Synthesis of multi-wavelength temporal phase-shifting algorithms optimized for high signal-to-noise ratio and high detuning robustness using the frequency transfer function

Manuel Servin<sup>\*</sup>, Moises Padilla and Guillermo Garnica

Centro de Investigaciones en Optica A. C., Loma del Bosque 115, Col. Lomas del Campestre, 37150 Leon Guanajuato, Mexico.

[mservin@cio.mx](mailto:mservin@cio.mx)

**Abstract:** Synthesis of single-wavelength temporal phase-shifting algorithms (PSA) for interferometry is well-known and firmly based on the frequency transfer function (FTF) paradigm. Here we extend the single-wavelength FTF-theory to dual and multi-wavelength PSA-synthesis when several simultaneous laser-colors are present. The FTF-based synthesis for dual-wavelength PSA (DW-PSA) is optimized for high signal-to-noise ratio and minimum number of temporal phase-shifted interferograms. The DW-PSA synthesis herein presented may be used for interferometric contouring of discontinuous industrial objects. Also DW-PSA may be useful for DW shop-testing of deep free-form aspheres. As shown here, using the FTF-based synthesis one may easily find explicit DW-PSA formulae optimized for high signal-to-noise and high detuning robustness. To this date, no general synthesis and analysis for temporal DW-PSAs has been given; only *had-hoc* DW-PSAs formulas have been reported. Consequently, no explicit formulae for their spectra, their signal-to-noise, their detuning and harmonic robustness has been given. Here for the first time a fully general procedure for designing DW-PSAs (or triple-wavelengths PSAs) with desire spectrum, signal-to-noise ratio and detuning robustness is given. We finally generalize DW-PSA to higher number of wavelength temporal PSAs.

09-March-2016 Centro de Investigaciones en Optica, Mexico.

**OCIS codes:** (120.0120) Instrumentation, measurement, and metrology; (120.6650) Surface measurements, figure; (100.2650) Fringe analysis.

---

## References and links

1. M. Servin, J. A. Quiroga, and M. Padilla, *Interferogram Analysis for Optical Metrology, Theoretical principles and applications* (Wiley-VCH, 2014).
2. J. Wyant, "Testing aspherics using two-wavelength holography," *Appl. Opt.* **10**, 2113–2118 (1971).
3. C. Polhemus, "Two-wavelength interferometry," *Appl. Opt.* **12**, 2071–2074 (1973).
4. Y. Y. Cheng and J.C. Wyant, "Multiple-wavelength phase-shifting interferometry," *Appl. Opt.* **24**, 804–807 (1985).
5. Y. Y. Cheng and J.C. Wyant, "Two-wavelength phase shifting interferometry," *Appl. Opt.* **23**, 4539–4543 (1984).
6. R. Onodera and Y. Ishii, "Two-wavelength interferometry that uses a Fourier-transform method," *Appl. Opt.* **37**, 7988–7994 (1998).
7. C. Wagner, W. Osten and S. Seebacher, "Direct shape measurement by digital wavefront reconstruction and multiwavelength contouring," *Opt. Eng.* **39**, 79–85 (2000).
8. J. Gass, A. Dakoff and M. Kim, "Phase imaging without  $2\pi$  ambiguity by multi-wavelength digital holography," *Opt. Lett.* **28**, 1141–1143 (2003).
9. S. De Nicola, A. Finizio, G. Pierattini, D. Alfieri, S. Grilli, L. Sansone, and P. Ferraro, "Recovering correct phase information in multiwavelength digital holographic microscopy by compensation for chromatic aberrations," *Opt. Lett.* **30**, 2706–2708 (2005).

10. J. Kühn, T. Colomb, F. Montfort, F. Charrière, Y. Emery, E. Cuhe, P. Marquet, and C. Depeursinge, "Real-time dual-wavelength digital holographic microscopy with a single hologram acquisition," *Opt. Express* **15**, 7231–7242 (2007).
11. K. Falaggis, D. P. Towers, and C. E. Towers, "Multiwavelength interferometry: extended range metrology," *Opt. Lett.* **34**, 950–952 (2009).
12. T. Kakue, Y. Moritani, K. Ito, Y. Shimozato, Y. Awatsuji, K. Nishio, S. Ura, T. Kubota, and O. Matoba, "Image quality improvement of parallel four-step phase-shifting digital holography by using the algorithm of parallel two-step phase-shifting digital holography," *Opt. Express* **18**, 9555–9560 (2010).
13. D. Abdelsalam, R. Magnusson, and D. Kim, "Single-shot, dual-wavelength digital holography based on polarizing separation," *Appl. Opt.* **50**, (2011) 3360–3368 (2011).
14. D. Abdelsalam and D. Kim, "Two-wavelength in-line phase-shifting interferometry based on polarizing separation for accurate surface profiling," *Appl. Opt.* **50**, 6153–6161 (2011).
15. U.P. Kumar, N.K. Mohan, and M. Kothiyal, "Red–Green–Blue wavelength interferometry and TV holography for surface metrology," *J. Opt.* **40**, 176–183 (2011).
16. D. Barada, T. Kiire, J.-i Sugisaka, S. Kawata, and T. Yatagai, "Simultaneous two-wavelength Doppler phase-shifting digital holography," *Appl. Opt.* **50**, H237–H244 (2011).
17. R. Kulkarni and P. Rastogi, "Multiple phase estimation in digital holographic interferometry using product cubic phase function," *Opt Laser Eng.* **51**, 1168–1172 (2013).
18. W. Zhang, X. Lu, L. Fei, H. Zhao, H. Wang, and L. Zhong, "Simultaneous phase-shifting dual-wavelength interferometry based on two-step demodulation algorithm," *Opt. Lett.* **39**, 5375–5378 (2014).
19. W. Zhang, X. Lu, C. Luo, L. Zhong, and J. Vargas, "Principal component analysis based simultaneous dual-wavelength phase-shifting interferometry," *Opt. Comm.* **341**, 276–283 (2015).

---

## 1. Introduction

As far as we know, the first researcher to use dual-wavelength (DW) interferometry was Wyant in 1971 [1]. Wyant used two fixed laser-wavelengths  $\lambda_1$  and  $\lambda_2$  to test an optical surface with an equivalent wavelength of  $\lambda_{eq} = \lambda_1 \lambda_2 / |\lambda_1 - \lambda_2|$  [2]. Thus typically  $\lambda_{eq}$  is much larger than either  $\lambda_1$  or  $\lambda_2$  ( $\lambda_{eq} \gg \{\lambda_1, \lambda_2\}$ ). Double-wavelength (DW) interferometry was improved by Polhemus [3] and Cheng [4,5] using digital temporal phase-shifting.

On the other hand, Onodera et al. [6] used spatial-carrier, double-wavelength digital-holography (DW-DH) and Fourier interferometry for phase-demodulation. This in turn was followed by a large number of multi-wavelength digital-holographic (DH) Fourier phase-demodulation methods in such diverse applications as interferometric contouring [7], phase-imaging [8], chromatic aberration compensation in microscopy [9]; single hologram DW microscopy [10]; comb multi-wavelength laser for extended range optical metrology [11], and a two-steps digital-holography for image quality improvement [12].

More recently temporal dual-wavelength phase-shifting algorithms (DW-PSAs) have been reworked by Abdelsalam et al. [14]. Even though Abdelsalam et al. give working PSA formulas they do not estimate their spectra, their signal-to noise ratio, or their detuning and harmonics robustness. Kumar [15] and Baranda [16] also provided valid temporal PSA formulas but also failed to characterize their PSAs in terms of signal-to-noise, detuning and harmonic rejection. Another different approach was followed by Kulkarni and Rastogi [16] in which they have demodulated the two interesting phases by fitting a low-order polynomial to each phase. Their approach [17] worked well for the example provided but we think their method could easily cross-talk between fitted polynomials for complicated modulating phases [17]. Yet another approach by Zhang et al. was published [18-19]. Zhang used a simultaneous two-steps [18], and principal component interferometry [19] to solve the dual-wavelength phase-shifting measurement. Zhang et al. used 32 randomly phase-shifted interferograms [19]. Even though Zhang [19] could demodulate the two phases, they used 32 phase-shifted temporal interferograms. All these works on temporal DW-PSA [2-5,14-19] have given just specific DW-PSAs without explicit formulae for their spectra, signal-to-noise, detuning and harmonic robustness.

In contrast to previous *ad-hoc* temporal DW-PSA formulas, here we give a general theory for synthesizing DW-PSAs formalizing their spectrum, their signal-to-noise, and their detuning-harmonic robustness. At the risk of being repetitive, we emphasize that we are not

just giving particular DW-PSAs formulas as previously done [2-5, 14-19]. Here we are giving a general FTF-theory for synthesizing DW-PSA giving with explicit formulae for the most important characteristics of any PSA: spectra, signal-to-noise, detuning and harmonic robustness.

## 2. Spatial-carrier phase-demodulation for Dual-wavelength (DW) interferometry

Dual-wavelength digital-holography (DW-DH) is well understood and widely used [6-10]. As shown in Fig. 1, in DW-DH the two lasers beams are tilted to introduce spatial-carrier fringes [7]. In Fig. 1 both lasers beams are tilted in the  $x$  direction, but in general, for a better use of the Fourier space, one may tilt them independently along the  $x$  and  $y$  directions [11-14].

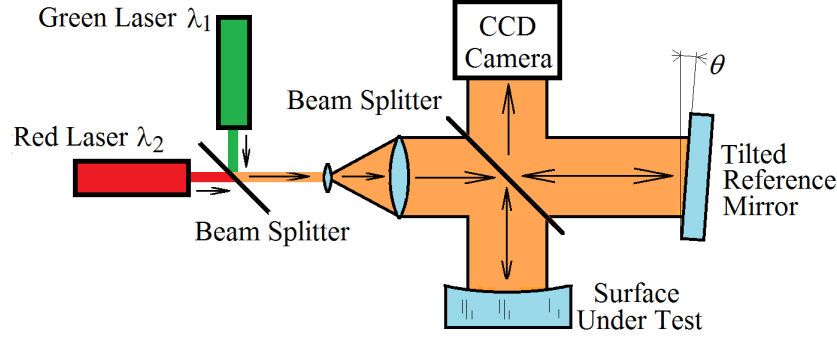


Fig.1 Schematics for DW-DH with a single tilted reference mirror [6]. The orange-light corresponds to the spatial superposition of the red and green lasers.

The DW-DH obtained at the CCD camera in Fig.1 may be modeled by,

$$I(x, y, t) = a(x, y) + b_1(x, y) \cos[\varphi_1(x, y) + u_1 x] + b_2(x, y) \cos[\varphi_2(x, y) + u_2 x]. \quad (1)$$

Here  $u_1 x = x(2\pi / \lambda_1) \tan(\theta)$  and  $u_2 x = x(2\pi / \lambda_2) \tan(\theta)$  are the spatial-carriers of the DW-DH. The reference mirror angle along the  $x$  axis is  $\theta$ . The searched phases are  $\varphi_1(x, y) = (2\pi / \lambda_1) W_1(x, y)$  and  $\varphi_2(x, y) = (2\pi / \lambda_2) W_2(x, y)$ ; being  $W_1(x, y)$  and  $W_2(x, y)$  the measuring wavefronts. Figure 2 shows a Fourier spectrum of Eq. (1).

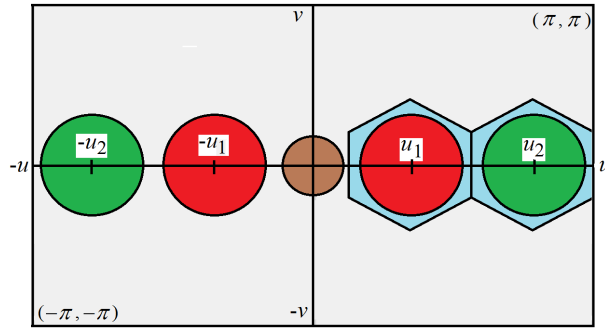


Fig. 2. The hexagons represent the spatial filters, which demodulate the phases  $\varphi_1$  and  $\varphi_2$ .

The two hexagons in Fig. 2 are the quadrature filters that passband the desired analytic signals. After filtering, the inverse Fourier transform find the demodulated phases [1]. The advantage of DW-DH is that only one digital-hologram is needed to obtain  $\{\varphi_1, \varphi_2\}$ ; however its drawback is that just a fraction of the Fourier space  $(u, v) \in [-\pi, \pi] \times [-\pi, \pi]$  is used (Fig 2). This limitation makes DW-DH not suitable for measuring discontinuous industrial objects [7]. In contrast, in DW-PSAs the full Fourier spectrum  $(u, v) \in [-\pi, \pi] \times [-\pi, \pi]$  may be used.

### 3. Dual-wavelength (DW) temporal-carrier phase-shifting interferometry

The temporal phase-shifting double-wave interferogram may be modeled as,

$$I(x, y, t) = a(x, y) + b_1(x, y) \cos \left[ \varphi_1(x, y) + \left( \frac{2\pi}{\lambda_1} d \right) t \right] + b_2(x, y) \cos \left[ \varphi_2(x, y) + \left( \frac{2\pi}{\lambda_2} d \right) t \right]. \quad (2)$$

Where  $t \in (-\infty, \infty)$ , and  $\varphi_1(x, y) = (2\pi / \lambda_1) W_1(x, y)$ ,  $\varphi_2(x, y) = (2\pi / \lambda_2) W_2(x, y)$  are the measuring phases. The parameter  $d$  is the PZT-step. The fringes background is  $a(x, y)$  and the lasers power must be about the same to obtain high fringe contrast:  $b_1(x, y) \approx b_2(x, y)$ . Figure 3 shows one possible set-up for a DW temporal phase-shifting interferometer.

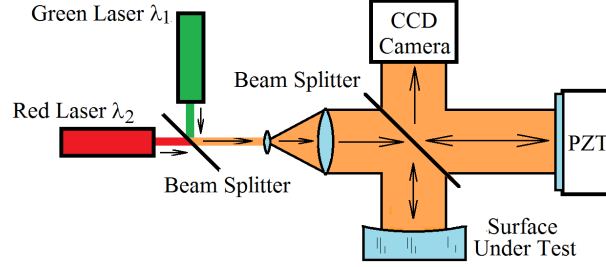


Fig. 3. A schematic example of a DW temporal-carrier interferometer [2-5] for surface measured with equivalent wavelength  $\lambda_{eq}$ ; the piezoelectric transducer is PZT.

The motivation of using 2-wavelengths  $\lambda_1$  and  $\lambda_2$  (in spatial or temporal interferometry) is that interferometric measurements can be made with an equivalent wavelength  $\lambda_{eq}$  [2-19],

$$\lambda_{eq} = \frac{\lambda_1 \lambda_2}{|\lambda_1 - \lambda_2|}; \quad \lambda_{eq} \gg (\lambda_1 \text{ or } \lambda_2). \quad (3)$$

With large  $\lambda_{eq}$  one may measure deeper surface discontinuities or topographies than using either  $\lambda_1$  or  $\lambda_2$  alone [2-19]. For a given PZT-step  $d$ , the two angular-frequencies (in radians per interferogram) are given by,

$$\omega_1 = \frac{2\pi}{\lambda_1} d, \quad \text{and} \quad \omega_2 = \frac{2\pi}{\lambda_2} d. \quad (4)$$

Using this equation one may rewrite Eq. (2) as,

$$I(x, y, t) = a(x, y) + b_1(x, y) \cos[\varphi_1(x, y) + \omega_1 t] + b_2(x, y) \cos[\varphi_2(x, y) + \omega_2 t], \quad (5)$$

Here we have 5 unknowns: namely,  $\{a, b_1, b_2, \varphi_1, \varphi_2\}$ . Therefore we need at least 5 phase-shifted interferograms to obtain a solution for  $\varphi_1(x, y)$  and  $\varphi_2(x, y)$ . These are given by:

$$\begin{aligned} I_0(x, y) &= a + b_1 \cos[\varphi_1] + b_2 \cos[\varphi_2], \\ I_1(x, y) &= a + b_1 \cos[\varphi_1 + \omega_1] + b_2 \cos[\varphi_2 + \omega_2], \\ I_2(x, y) &= a + b_1 \cos[\varphi_1 + 2\omega_1] + b_2 \cos[\varphi_2 + 2\omega_2], \\ I_3(x, y) &= a + b_1 \cos[\varphi_1 + 3\omega_1] + b_2 \cos[\varphi_2 + 3\omega_2], \\ I_4(x, y) &= a + b_1 \cos[\varphi_1 + 4\omega_1] + b_2 \cos[\varphi_2 + 4\omega_2]. \end{aligned} \quad (6)$$

For clarity, most  $(x, y)$  coordinates were omitted.

#### 4. Fourier-spectrum for temporal DW-PSAs

The Fourier transform of the temporal interferogram (with  $t \in (-\infty, \infty)$ ) in Eq. (5) is:

$$I(\omega) = a \delta(\omega) + \frac{b_1}{2} \left[ e^{i\varphi_1} \delta(\omega - \omega_1) + e^{-i\varphi_1} \delta(\omega + \omega_1) \right] + \frac{b_2}{2} \left[ e^{i\varphi_2} \delta(\omega - \omega_2) + e^{-i\varphi_2} \delta(\omega + \omega_2) \right]. \quad (7)$$

All  $(x, y)$  were omitted. As mentioned,  $\omega_1 = (2\pi / \lambda_1)d$  and  $\omega_2 = (2\pi / \lambda_2)d$  are the two temporal-carrier frequencies in radians/interferogram; Fig. 4 shows this spectrum.

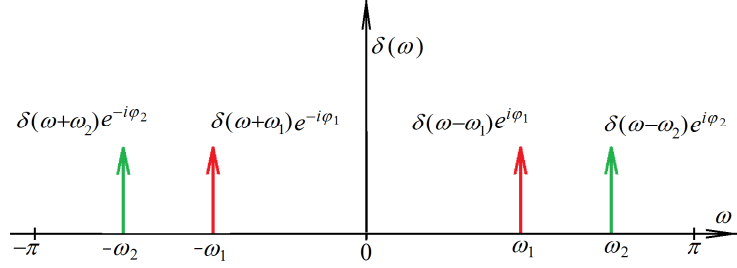


Fig. 4. Fourier spectrum of the DW temporal-carrier interferograms.

Figure 5 shows two ideal quadrature filters  $H_1(\omega)$  and  $H_2(\omega)$  that could passband the desired analytic signals  $\delta(\omega - \omega_1)\exp(i\varphi_1)$  and  $\delta(\omega - \omega_2)\exp(i\varphi_2)$ . Note how each filter is able to passband the desired signals from the same temporal interferograms.

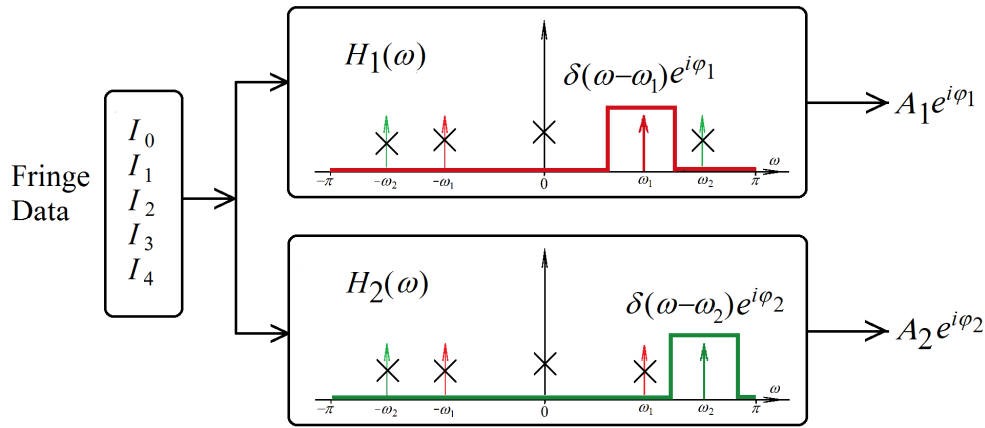


Fig. 5. Ideal spectra of two filters that passband the desired signals  $\exp(i\varphi_1)$  and  $\exp(i\varphi_2)$  from temporal phase-shifted interferograms; all crossed Dirac deltas are filtered-out.

#### 5. Synthesis of DW-PSAs using 5-step temporal interferograms

The rectangular filters in Fig. 5 require a large number of temporal interferograms [1]. However, using the FTF we can synthesize 5-step bandpass filters by allocating 4 spectral-zeros at frequencies  $\{-\omega_2, -\omega_1, 0, \omega_2\}$  for  $H_1(\omega)$ , and at  $\{-\omega_2, -\omega_1, 0, \omega_1\}$  for  $H_2(\omega)$  as,

$$\begin{aligned} H_1(\omega) &= (1 - e^{i\omega}) [1 - e^{i(\omega+\omega_2)}] [1 - e^{i(\omega-\omega_2)}] [1 - e^{i(\omega+\omega_1)}], \\ H_2(\omega) &= (1 - e^{i\omega}) [1 - e^{i(\omega-\omega_1)}] [1 - e^{i(\omega+\omega_1)}] [1 - e^{i(\omega+\omega_2)}]. \end{aligned} \quad (8)$$

From Eq. (8) one sees that by design,  $I(\omega)H_1(\omega)$  passband the signal  $\exp(i\varphi_1)\delta(\omega-\omega_1)$ , while  $I(\omega)H_2(\omega)$  bandpass  $\exp(i\varphi_2)\delta(\omega-\omega_2)$ . The impulse responses  $h_1(t)$  and  $h_2(t)$  of these two quadrature filters are then given by:

$$\begin{aligned} h_1(t) &= F^{-1}\{H_1(\omega)\} = \sum_{n=0}^4 c1_n(\omega_1, \omega_2) \delta(t-n), \\ h_2(t) &= F^{-1}\{H_2(\omega)\} = \sum_{n=0}^4 c2_n(\omega_1, \omega_2) \delta(t-n). \end{aligned} \quad (9)$$

Here  $c1_n(\omega_1, \omega_2)$  and  $c2_n(\omega_1, \omega_2)$  are complex-valued coefficients that depend on the frequencies  $\{\omega_1, \omega_2\}$ . Having  $h_1(t)$  and  $h_2(t)$ , we obtain the two searched DW-PSAs as,

$$\begin{aligned} \frac{1}{2} H_1(\omega_1) b(x, y) e^{i\varphi_1(x, y)} &= \sum_{n=0}^4 c1_n(\omega_1, \omega_2) I_n(x, y), \\ \frac{1}{2} H_2(\omega_2) b(x, y) e^{i\varphi_2(x, y)} &= \sum_{n=0}^4 c2_n(\omega_1, \omega_2) I_n(x, y). \end{aligned} \quad (10)$$

The explicit 5-step DW-PSA formula to estimate  $\varphi_1(x, y)$  is:

$$\begin{aligned} A_1 \exp(i\varphi_1) &= -e^{i\omega_2} I_0 + c1_1(\omega_1, \omega_2) I_1 - c1_2(\omega_1, \omega_2) I_2 + c1_3(\omega_1, \omega_2) I_3 - e^{i(\omega_2-\omega_1)} I_4, \\ c1_1(\omega_1, \omega_2) &= 1 + e^{i\omega_2} + e^{2i\omega_2} + e^{i(\omega_2-\omega_1)}, \\ c1_2(\omega_1, \omega_2) &= 1 + e^{i\omega_2} + e^{2i\omega_2} + e^{i(\omega_2-\omega_1)} + e^{-i\omega_1} + e^{i(2\omega_2-\omega_1)}, \\ c1_3(\omega_1, \omega_2) &= [1 + e^{-i\omega_1} + e^{-i(\omega_2+\omega_1)} + e^{i(\omega_2-\omega_1)}] e^{i\omega_2}. \end{aligned} \quad (11)$$

Being  $A_1 = (1/2)H_1(\omega_1)b(x, y)$ . Conversely the 5-step DW-PSA to estimate  $\varphi_2(x, y)$  is:

$$\begin{aligned} A_2 \exp(i\varphi_2) &= -e^{i\omega_1} I_0 + c2_1(\omega_1, \omega_2) I_1 - c2_2(\omega_1, \omega_2) I_2 + c2_3(\omega_1, \omega_2) I_3 - e^{i(\omega_1-\omega_2)} I_4, \\ c2_1(\omega_1, \omega_2) &= 1 + e^{i\omega_1} + e^{2i\omega_1} + e^{i(\omega_1-\omega_2)}, \\ c2_2(\omega_1, \omega_2) &= 1 + e^{i\omega_1} + e^{2i\omega_1} + e^{i(\omega_1-\omega_2)} + e^{-i\omega_2} + e^{i(2\omega_1-\omega_2)}, \\ c2_3(\omega_1, \omega_2) &= [1 + e^{-i\omega_2} + e^{-i(\omega_1+\omega_2)} + e^{i(\omega_1-\omega_2)}] e^{i\omega_1}. \end{aligned} \quad (12)$$

Being  $A_2 = (1/2)H_2(\omega_2)b(x, y)$ . This is the basics for synthesizing DW-PSAs grounded on the FTF paradigm [1]. Previous papers on DW-PSAs [2-5,14-19] stop much shorter than this. They just show particular pairs of DW-PSAs [2-5,14-19] that work for just particular carriers, *i.e.*  $(\omega_1, \omega_2) = (1.2, 2.9)$ . In this section, we offered DW-PSAs (Eqs. (11)-(12)) which work well (find  $\varphi_1$  and  $\varphi_2$ ) for infinitely-continuous frequency-pairs  $(\omega_1, \omega_2) \in [-\pi, \pi] \times [-\pi, \pi]$ . Even if the theory of this paper would stop right here, this paper would contain a substantial improvement against current *ad-hoc* art in DW-PSA [2-5,14-19].

## 6. Signal-to-noise power-ratios for $H_1(\omega)$ and $H_2(\omega)$

Here we review the signal-to-noise power-ratio formulas for PSA quadrature filters [1]. The signal-to-noise power-ratios for  $H_1(\omega)$  and  $H_2(\omega)$  are given by [1]:

$$SNR_1 = \frac{|H_1(\omega_1)|^2}{\frac{1}{2\pi} \int_{-\pi}^{\pi} |H_1(\omega)|^2 d\omega}, \quad SNR_2 = \frac{|H_2(\omega_2)|^2}{\frac{1}{2\pi} \int_{-\pi}^{\pi} |H_2(\omega)|^2 d\omega}. \quad (13)$$

These 2 *SNR*-formulas give the power of the demodulated signals  $|H_1(\omega_1)|^2$  and  $|H_2(\omega_2)|^2$  divided by their total noise-power  $(1/2\pi)\int |H_1(\omega)|^2 d\omega$  and  $(1/2\pi)\int |H_2(\omega)|^2 d\omega$ .

### 7. Non-optimized DW-PSA design for wavelengths $\lambda_1 = 632.8\text{nm}$ and $\lambda_2 = 532.0\text{nm}$

Let us assume that we use a typical temporal frequency of  $\omega_1 = 2\pi/5$  radians per sample for the algorithm  $H_1(\omega_1)e^{i\varphi_1(x,y)}$ . Having made this choice for  $\omega_1$ , the frequency  $\omega_2$  is set to

$$d = \omega_1 \left( \frac{\lambda_1}{2\pi} \right) = \omega_2 \left( \frac{\lambda_2}{2\pi} \right) \Rightarrow \omega_2 = \omega_1 \left( \frac{\lambda_1}{\lambda_2} \right) \therefore \omega_2 = 1.49 \frac{\text{radians}}{\text{sample}}, \quad (14)$$

and the required PZT-step is  $d = 126.6\text{nm}$ . The DW-FTFs for these two frequencies are:

$$\begin{aligned} H_1(\omega) &= (1 - e^{i\omega}) [1 - e^{i(\omega+1.49)}] [1 - e^{i(\omega-1.49)}] [1 - e^{i(\omega+1.26)}], \\ H_2(\omega) &= (1 - e^{i\omega}) [1 - e^{i(\omega-1.26)}] [1 - e^{i(\omega+1.26)}] [1 - e^{i(\omega+1.49)}]. \end{aligned} \quad (15)$$

Figure 6 shows the magnitude plot of these two quadrature filters  $H_1(\omega)$  and  $H_2(\omega)$ .

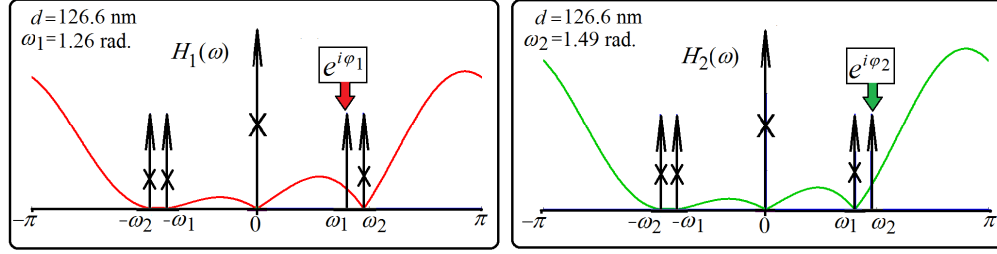


Fig. 6 Spectral plots for the two DW-PSA. The crossed Dirac deltas are the filter-out signals. These two FTFs can demodulate  $\varphi_1$  and  $\varphi_2$  but with poor signal-to-noise performance.

The signal-to-noise [1] for the searched signals  $H_1(\omega_1) \exp(i\varphi_1)$  and  $H_2(\omega_2) \exp(i\varphi_2)$  are,

$$\frac{|H_1(\omega_1)|^2}{\frac{1}{2\pi} \int_{-\pi}^{\pi} |H_1(\omega)|^2 d\omega} = 0.94; \quad \frac{|H_2(\omega_2)|^2}{\frac{1}{2\pi} \int_{-\pi}^{\pi} |H_2(\omega)|^2 d\omega} = 1.04; \quad \omega_1 = 1.26; \quad \omega_2 = 1.49. \quad (16)$$

For comparison, a 5-step least-squares PSA has a signal-to-noise power-ratio of 5 [1]. Thus  $\omega_1 = 2\pi/5$  and  $\omega_2 = 1.49$  were a bad choice; we can estimate  $\varphi_1(x,y)$  and  $\varphi_2(x,y)$  from the DW-PSAs in Eq. (11)-(12) using these temporal frequencies, but they are going to be noisy. Previous DW-PSAs efforts [2-5,14-19] only provide numeric-specific DW-PSAs formulas to obtain  $\varphi_1(x,y)$  and  $\varphi_2(x,y)$ . However, they were silent about their Fourier spectra; their signal-to-noise; their harmonics rejection and their detuning robustness. All this useful and practical formulae are given here for the first time in terms of the FTF for designing DW-PSAs. Moreover, in contrast to previous art in DW-PSAs, Eq. (11) and Eq. (12) give infinite DW-PSA formulas for continuous pairs of temporal frequencies  $(\omega_1, \omega_2) \in [-\pi, \pi] \times [-\pi, \pi]$ .

### 8. Optimized joint signal-to-noise ratio synthesis for DW-PSAs

To find a better selection for  $\omega_1 = (2\pi/\lambda_1)d$  and  $\omega_2 = (2\pi/\lambda_2)d$ , we construct a joint signal-to-noise ratio as,

$$G_{S/N}(d) = \left( \frac{|H_1(\omega_1)|^2}{\frac{1}{2\pi} \int_{-\pi}^{\pi} |H_1(\omega)|^2 d\omega} \right) \left( \frac{|H_2(\omega_2)|^2}{\frac{1}{2\pi} \int_{-\pi}^{\pi} |H_2(\omega)|^2 d\omega} \right); \quad d \in [0, \lambda_{eq}]. \quad (17)$$

The function  $G_{S/N}(d)$  is complicated and has many local maxima but, fortunately, it is one-dimensional. Thus we plot  $G_{S/N}(d)$  and look for a good maximum, and take the PZT-step  $d$ . This PZT-step  $d$  is used to find the two specific DW-PSA (Eqs. (11)-(12)) which solves the dual-wavelength interferometric problem.

### 9. Example of optimized DW-PSA synthesis for $\lambda_1 = 632.8\text{nm}$ and $\lambda_2 = 532\text{nm}$

The graph for the joint signal-to-noise ratio  $G_{S/N}(d)$  with  $\omega_1 = (2\pi / \lambda_1)d$ ,  $\omega_2 = (2\pi / \lambda_2)d$  and  $d \in [0, \lambda_{eq}]$  is shown next.

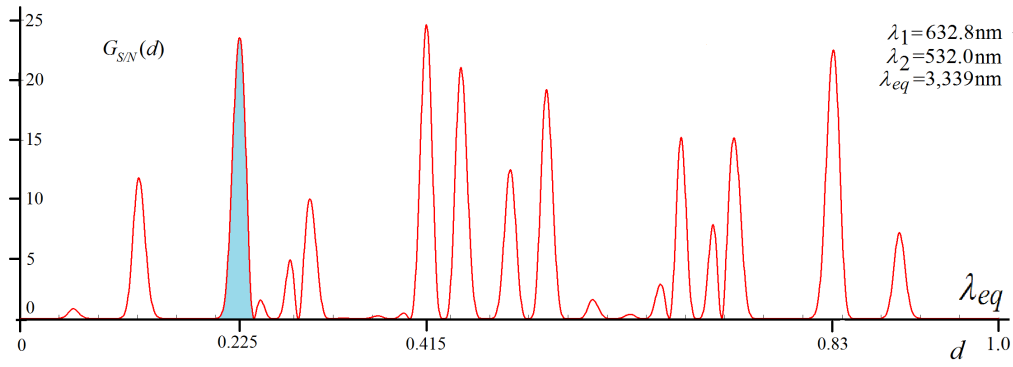


Fig. 7. Graph of  $G_{S/N}(d)$ . We kept the third local maximum at  $d = 0.225\lambda_{eq} = 751\text{nm}$ , for which  $G_{S/N}(d) = 23.5$ . Each DW-PSA thus have a signal-to-noise of  $\sqrt{23.5} \approx 4.84$ .

The first good-enough maximum is  $G_{S/N}(0.225\lambda_{eq}) \approx 23.5$  (in blue), being  $d = 0.225\lambda_{eq}$  or  $d = 751\text{nm}$ . Note that most of this graph is less than 20; i.e.  $G_{S/N}(d) < 20$ . This means that taking a PZT-step within  $d \in [0, \lambda_{eq}]$  at random, the probability of landing in a very low signal-to-noise point is very high.

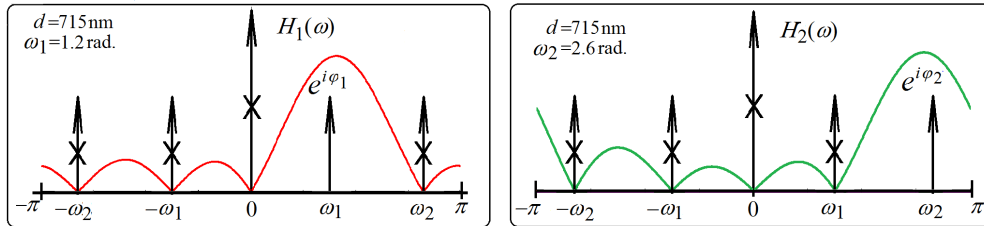


Fig. 8. Spectral plots for  $H_1(\omega)$  and  $H_2(\omega)$  for the  $S/N$ -optimized DW-PSA. Note that  $\omega_1 = W[(2\pi / \lambda_1)d] = 1.2$  and  $\omega_2 = W[(2\pi / \lambda_2)d] = 2.6$ ; with  $W(x) = \arg[\exp(ix)]$ .

Therefore in this section we have shown that even though the correct phases  $\phi_1(x, y)$  and  $\phi_2(x, y)$  can be found using Eq. (11) and Eq. (12), without plotting  $G_{S/N}(d)$  these DW-PSAs designs will have a low signal-to-noise power-ratio with high probability.



### 9. Example for DW-PSA phase-demodulation for $\lambda_1 = 632.8\text{nm}$ and $\lambda_2 = 532.0\text{nm}$

Figure 9 shows five computer-simulated interferograms to test the DW-PSAs found in previous section. The PZT-step is  $d = 751\text{nm}$ , giving a good signal-to-noise ratio. As mentioned, for large PZT-steps, the angular frequencies  $(\omega_1, \omega_2)$  are wrapped and given by,

$$\omega_1 = \arg[\exp(i d 2\pi / \lambda_1)] = 2.6, \quad \omega_2 = \arg[\exp(i d 2\pi / \lambda_2)] = 1.2 \quad (18)$$

Using these angular frequencies in Eq. (11), the specific formula to estimate  $\phi_1(x, y)$  is,

$$A_1(\omega_1)e^{i\phi_1} = -e^{2.6i}I_0 + (0.78 + 0.62i)I_1 - (0.5 - i)I_2 - (1 + 0.19i)I_3 - e^{-1.4i}I_4 \quad (19)$$

Also, from Eq. (12), the specific 5-step DW-PSA to estimate the signal  $\phi_2(x, y)$  is,

$$A_2(\omega_2)e^{i\phi_2} = -e^{1.2i}I_0 + (0.8 + 0.6i)I_1 - (0.92 - 0.1i)I_2 + (0.65 - 0.77i)I_3 - e^{1.4i}I_4. \quad (20)$$

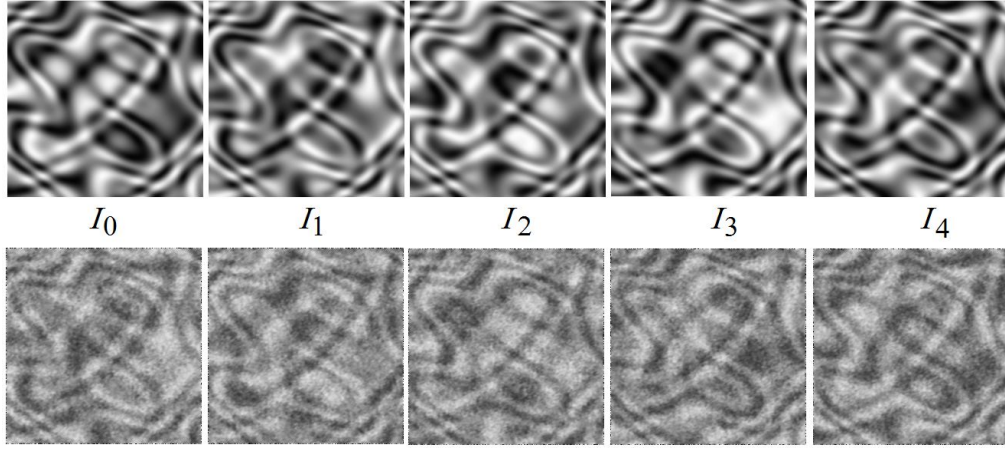


Fig. 9. The upper row shows 5 simulated interferograms without noise. The lower panel shows the same interferograms corrupted with phase-noise uniformly distributed in  $[0, \pi]$ . The noisy fringes were low-pass filtered by a 3x3 averaging window.

Figure 10 shows the demodulated signals  $\phi_1(x, y)$  and  $\phi_2(x, y)$ .

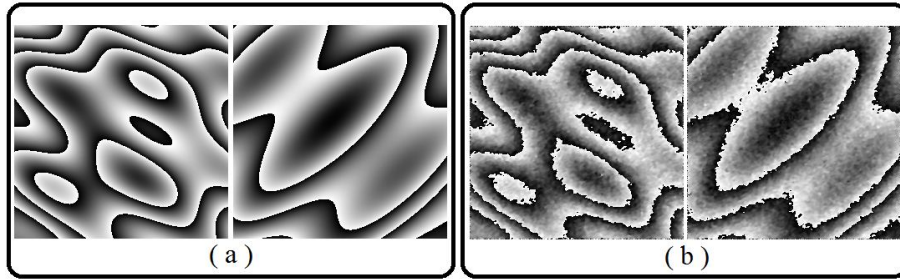


Fig. 10. The demodulated phases  $\phi_1(x, y)$  and  $\phi_2(x, y)$  corresponding to the noiseless (panel (a)) and noisy (panel (b)) 5-steps interferograms in Fig. 9. Please note that there is no cross-tacking between the two demodulated phases  $\phi_1(x, y)$  and  $\phi_2(x, y)$ .

Figure 10(a) shows the noiseless demodulated phases, while Fig. 10(b) shows the demodulated phases degraded with a phase noise uniformly distributed within  $[0, \pi]$ . Note that absolutely no cross-talking between the demodulated phases  $\varphi_1$  and  $\varphi_2$  appears.

### 10. Detuning-robust DW-PSA synthesis for $\lambda_1 = 632.8\text{nm}$ and $\lambda_2 = 458\text{nm}$

Let us assume that our PZT is poorly calibrated. Thus instead of having well-tuned frequencies at  $\{\omega_1, \omega_2\}$  we have detuned frequencies at  $\{\omega_1 + \Delta, \omega_2 + \Delta\}$ , being  $\Delta$  the amount of detuning. As Fig. 11 shows, the estimated phase  $\hat{\varphi}_2(x, y)$  is now be given by,

$$A_2 e^{-i\hat{\varphi}_2} = H_2(\omega_1 + \Delta) e^{-i\varphi_1} + H_2(\omega_2 + \Delta) e^{-i\varphi_2} + H_2(\omega_1 - \Delta) e^{i\varphi_1} + H_2(\omega_2 - \Delta) e^{i\varphi_2}. \quad (21)$$

The estimated phase  $\hat{\varphi}_2(x, y)$  then have cross-talking from  $\{e^{-i\varphi_1}, e^{i\varphi_1}, e^{-i\varphi_2}\}$ ; conversely  $\hat{\varphi}_1(x, y)$  will be distorted by cross-talking from  $\{e^{-i\varphi_2}, e^{i\varphi_2}, e^{-i\varphi_1}\}$ .

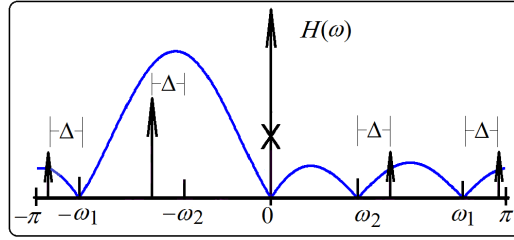


Fig. 11. Here we show the effect of detuning ( $\Delta$ ), greatly exaggerated for clarity. The amount of linear detuning is  $\Delta$  (radians/sample). The well-tuned frequencies are  $\{-\omega_2, -\omega_2, \omega_1, \omega_2\}$ , while the detuned frequencies are  $\{-\omega_2 - \Delta, -\omega_2 - \Delta, \omega_1 + \Delta, \omega_2 + \Delta\}$ .

To ensure good detuning robustness we need double-zeroes at the rejected frequencies. Therefore, we transform Eq. (8) (5-steps) to detuning-robust DW-FTFs (8-steps) as,

$$\begin{aligned} H_1(\omega) &= (1 - e^{i\omega}) [1 - e^{i(\omega+\omega_2)}]^2 [1 - e^{i(\omega-\omega_2)}]^2 [1 - e^{i(\omega+\omega_1)}]^2, \\ H_2(\omega) &= (1 - e^{i\omega}) [1 - e^{i(\omega-\omega_1)}]^2 [1 - e^{i(\omega+\omega_1)}]^2 [1 - e^{i(\omega+\omega_2)}]^2. \end{aligned} \quad (22)$$

Next, we plot  $G_{S/N}(d)$  and look for a high local signal-to-noise maximum; see Fig. 12.

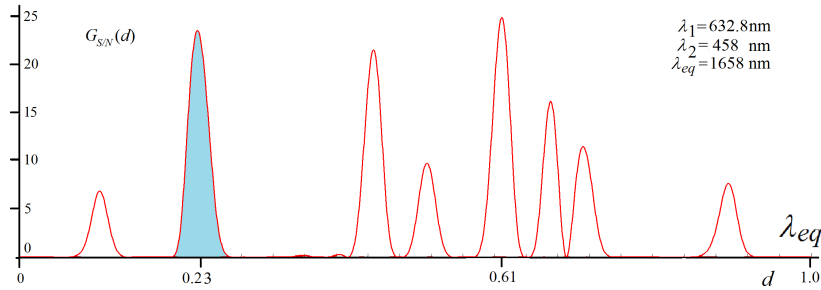


Fig. 12. Graph of the joint signal-to-noise power-ratio  $G_{S/N}(d)$  of the two detuning-robust FTF-filters in Eq. (22). The second maximum has a PZT-displacement of  $d=381\text{nm}$ .

We choose the second maximum (in blue) where  $G_{S/N}(0.23\lambda_{eq}) = 44$ , and  $d = 381\text{nm}$ . Each (8-steps) DW-PSA filter in Eq. (22) has a signal-to-noise ratio of about  $\sqrt{44} = 6.6$ . Figure 13

shows the two 8-step DW-PSA detuning-robust FTFs. The spectral second-order zeroes are flatter, so they are frequency detuning  $\Delta$  tolerant.

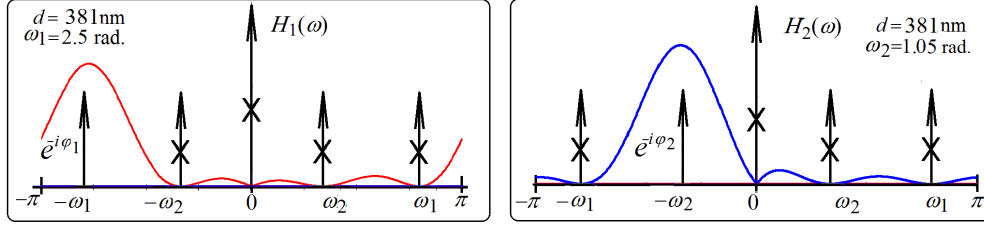


Fig. 13. Spectra of detuning-robust DW-PSA tuned at  $\omega_1=2.5\text{rad}$  and  $\omega_2=1.05\text{rad}$ . The second-order zeroes tolerate a fair amount of frequency detuning  $\Delta$ .

### 11. Harmonic rejection in DW-PSAs

Figure 14 shows the harmonic response for the FTFs in Eq. (8). The red-sticks are the fringe harmonics at  $(n\omega_1)$ , and the green ones are the fringe harmonics at  $(n\omega_2)$ ,  $|n| \geq 2$ .

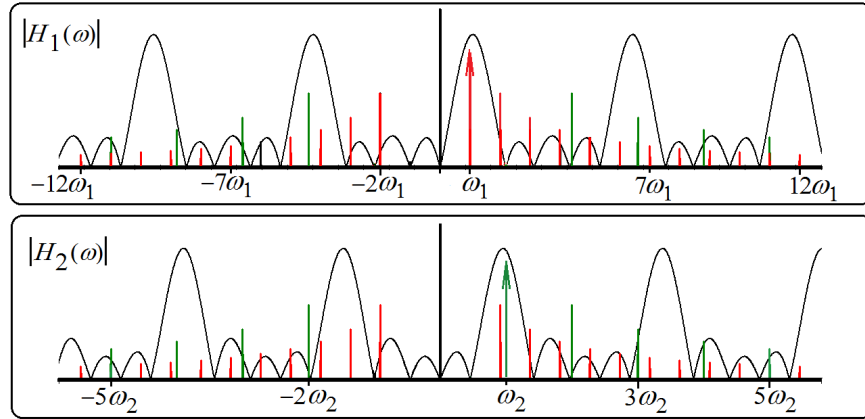


Fig. 14. Amplitudes of the distorting harmonics for  $|H_1(n\omega_1)|$ , in red; and  $|H_2(n\omega_2)|$ , in green. The ideal result would be to bandpass just the Dirac's deltas at  $\omega = \omega_1$  and  $\omega = \omega_2$ .

The power of the desired analytic signals  $|H_1(\omega_1)\exp(\varphi_1)|^2$  and  $|H_2(\omega_2)\exp(\varphi_2)|^2$  with respect to the distorting harmonics is given by,

$$\begin{aligned}
 HR_1 &= \frac{|H_1(\omega_1)|^2}{\sum_{|n| \geq 2} \left\{ \left( \frac{1}{n^2} \right)^2 \left[ |H_1(n\omega_1)|^2 + |H_2(n\omega_2)|^2 \right] \right\}} = 11.83, \\
 HR_2 &= \frac{|H_2(\omega_2)|^2}{\sum_{|n| \geq 2} \left\{ \left( \frac{1}{n^2} \right)^2 \left[ |H_1(n\omega_1)|^2 + |H_2(n\omega_2)|^2 \right] \right\}} = 12.2
 \end{aligned} \tag{23}$$

Here we assumed that the amplitude of the harmonics decreases as  $(1/n^2)$ , so their power decreases as  $(1/n^2)^2$ . With this assumption,  $H_1(\omega_1)$  and  $H_2(\omega_2)$  have about 10-times more power than the total power sum of their harmonics  $\{H_1(n\omega_1), H_1(n\omega_2), H_2(n\omega_1), H_2(n\omega_2)\}$ .

Figure 15 shows five saturated phase-shifted interferograms. These 5 temporal interferograms are then phase demodulated using DW-PSAs, Eqs (11)-(12).

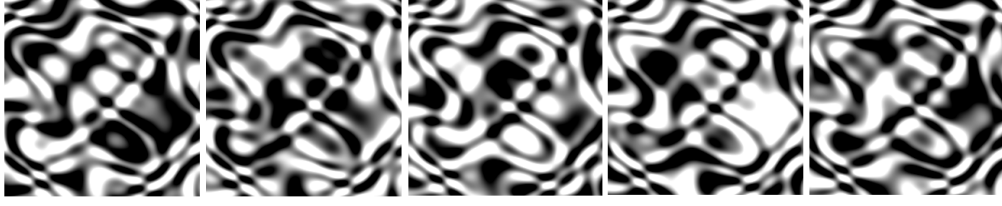


Fig. 15. Five DW phase-shifted temporal interferograms with amplitude saturation.

Figure 16 shows the demodulated phases  $\varphi_1$  and  $\varphi_2$  of the interferograms in Fig. 15.

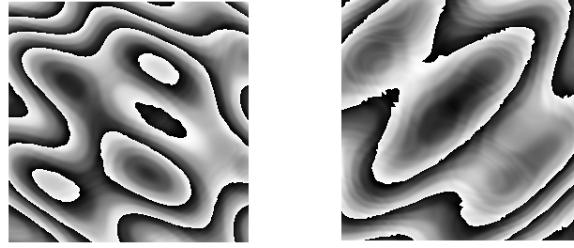


Fig. 16. The two demodulated phases from the 5 saturated fringe patterns in Fig. 15.

## 12. Multi-wavelength $\{\lambda_1, \lambda_2, \lambda_3, \dots, \lambda_n\}$ temporal phase-shifting interferometry

Here DW-PSA is generalized to 3-wavelengths. A simplified schematic of an interferometer simultaneously illuminated with 3-wavelengths  $\{\lambda_1, \lambda_2, \lambda_3\}$  is shown in Fig. 17.

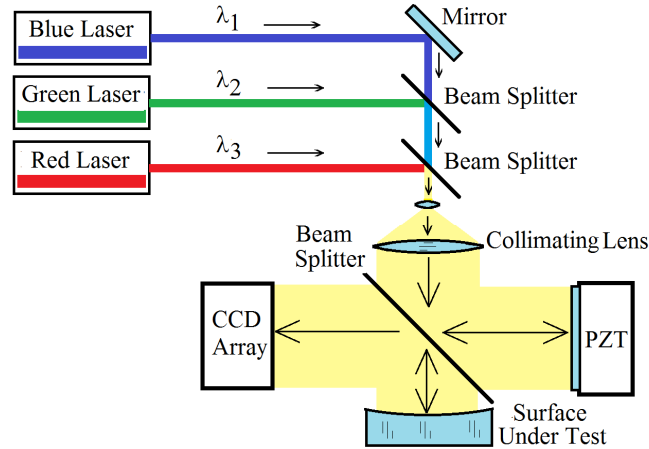


Fig. 17. Simplified schematics for a temporal 3-wavelength phase-shifting interferometer.

The continuous-time phase-shifted interferogram is,

$$I(x, y, t) = a + b_1 \cos[\varphi_1 + \omega_1 t] + b_2 \cos[\varphi_2 + \omega_2 t] + b_3 \cos[\varphi_3 + \omega_3 t]. \quad (24)$$

Now we have 7 unknowns  $\{a, b_1, b_2, b_3, \varphi_1, \varphi_2, \varphi_3\}$ ; being  $\{\varphi_1, \varphi_2, \varphi_3\}$  the searched phases. Thus we need at least 7 temporal phase-shifted interferograms. Figure 18 shows the Fourier spectrum of this 3-wavelengths interferogram.

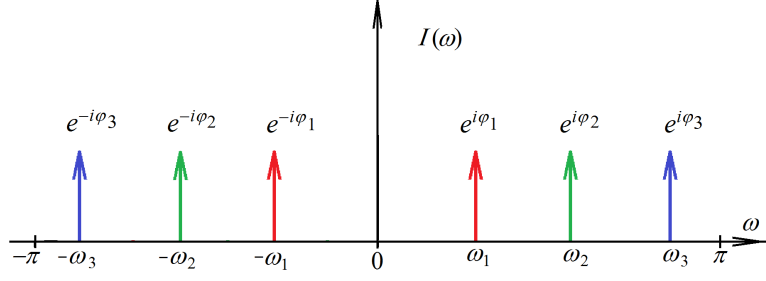


Fig. 18. Fourier spectrum  $I(\omega)$  for a 3-wavelength temporal phase-shifted interferogram.

Therefore we need to construct 3-FTFs having at least 6 first-order zeroes (7-steps) as,

$$\begin{aligned} H_1(\omega) &= (1 - e^{i\omega}) [1 - e^{i(\omega+\omega_2)}] [1 - e^{i(\omega-\omega_2)}] [1 - e^{i(\omega+\omega_3)}] [1 - e^{i(\omega-\omega_3)}] [1 - e^{i(\omega+\omega_1)}], \\ H_2(\omega) &= (1 - e^{i\omega}) [1 - e^{i(\omega-\omega_1)}] [1 - e^{i(\omega+\omega_1)}] [1 - e^{i(\omega+\omega_3)}] [1 - e^{i(\omega-\omega_3)}] [1 - e^{i(\omega+\omega_2)}], \\ H_3(\omega) &= (1 - e^{i\omega}) [1 - e^{i(\omega-\omega_1)}] [1 - e^{i(\omega+\omega_1)}] [1 - e^{i(\omega+\omega_2)}] [1 - e^{i(\omega-\omega_2)}] [1 - e^{i(\omega+\omega_3)}]. \end{aligned} \quad (25)$$

The spectrum  $H_1(\omega)$  rejects the analytic signals at  $\{-\omega_3, -\omega_2, -\omega_1, 0, \omega_2, \omega_3\}$ ;  $H_2(\omega)$  rejects the signals at  $\{-\omega_3, -\omega_2, -\omega_1, 0, \omega_1, \omega_3\}$ ; and  $H_3(\omega)$  rejects the analytic signals at  $\{-\omega_3, -\omega_2, -\omega_1, 0, \omega_1, \omega_2\}$ . Therefore  $I(\omega)H_1(\omega)$  passband  $\exp(i\varphi_1)\delta(\omega - \omega_1)$ ;  $I(\omega)H_2(\omega)$  passband  $\exp(i\varphi_2)\delta(\omega - \omega_2)$ , and finally  $I(\omega)H_3(\omega)$  passband  $\exp(i\varphi_3)\delta(\omega - \omega_3)$ .

The joint signal-to-noise power-ratio optimizing criterion now reads,

$$G_{S/N}(d) = \left( \frac{|H_1(\omega_1)|^2}{\frac{1}{2\pi} \int_{-\pi}^{\pi} |H_1(\omega)|^2 d\omega} \right) \left( \frac{|H_2(\omega_1)|^2}{\frac{1}{2\pi} \int_{-\pi}^{\pi} |H_2(\omega)|^2 d\omega} \right) \left( \frac{|H_3(\omega_3)|^2}{\frac{1}{2\pi} \int_{-\pi}^{\pi} |H_3(\omega)|^2 d\omega} \right). \quad (26)$$

We then find a convenient local maximum for  $G_{S/N}(d)$ , obtaining a fixed PZT-step  $d$ , and three angular-frequencies  $(\omega_1, \omega_2, \omega_3) \in [-\pi, \pi] \times [-\pi, \pi] \times [-\pi, \pi]$  as,

$$\omega_1 = W\left(\frac{2\pi}{\lambda_1}d\right), \quad \omega_2 = W\left(\frac{2\pi}{\lambda_2}d\right), \quad \omega_3 = W\left(\frac{2\pi}{\lambda_3}d\right); \quad W(x) = \arg[\exp(ix)]. \quad (27)$$

The three impulse responses  $\{h_1(t), h_2(t), h_3(t)\}$  are then given by,

$$\begin{aligned} h_1(t) &= F^{-1}\{H_1(\omega)\} = \sum_{n=0}^6 c1_n(\omega_1, \omega_2, \omega_3) \delta(t-n), \\ h_2(t) &= F^{-1}\{H_2(\omega)\} = \sum_{n=0}^6 c2_n(\omega_1, \omega_2, \omega_3) \delta(t-n), \\ h_3(t) &= F^{-1}\{H_3(\omega)\} = \sum_{n=0}^6 c3_n(\omega_1, \omega_2, \omega_3) \delta(t-n), \end{aligned} \quad (28)$$

Here  $c1_n(\omega_1, \omega_2, \omega_3)$ ,  $c2_n(\omega_1, \omega_2, \omega_3)$ ,  $c3_n(\omega_1, \omega_2, \omega_3)$  are the complex coefficients of the PSAs, which now depend on the three temporal-carrier frequencies  $\{\omega_1, \omega_2, \omega_3\}$ .

We now digitally grab 7 phase-shifted interferograms given by:

$$I_n = a + b_1 \cos[\varphi_1 + n\omega_1] + b_2 \cos[\varphi_2 + n\omega_2] + b_3 \cos[\varphi_3 + n\omega_3]; \quad n = 0, \dots, 6. \quad (29)$$

Obtaining the three searched quadrature analytic signals as,

$$\begin{aligned}
A_1(x, y) \exp[i \varphi_1(x, y)] &= \sum_{n=0}^6 c1_n(\omega_1, \omega_2, \omega_3) I_n(x, y), \\
A_2(x, y) \exp[i \varphi_2(x, y)] &= \sum_{n=0}^6 c2_n(\omega_1, \omega_2, \omega_3) I_n(x, y), \\
A_3(x, y) \exp[i \varphi_2(x, y)] &= \sum_{n=0}^6 c3_n(\omega_1, \omega_2, \omega_3) I_n(x, y),
\end{aligned} \tag{30}$$

where  $A_n(x, y) = (1/2)H_n(\omega_n)b(x, y)$ . By mathematical induction, one may see that a 4-wavelength  $\{\lambda_1, \lambda_2, \lambda_3, \lambda_4\}$  phase-shifting algorithm would need at least 9 phase-shifted interferograms, requiring FTFs having 8 first-order zeroes, etc, etc.

### 13. Conclusions

The problem that was solved here may be stated as follows: Having a laser interferometer simultaneously illuminated with fixed wavelengths  $\{\lambda_1, \lambda_2, \dots, \lambda_K\}$  and a single PZT phase-shifter, find  $K$  phase-shifting algorithms (PSAs) which phase-demodulate  $\{\varphi_1, \varphi_2, \dots, \varphi_K\}$  for each laser-color, with high signal-to-noise and no cross-taking among these phases.

This was solved as follows (for  $K=2$ , and  $K=3$  in section 12),

- a) To start, we synthesize two 5-step quadrature-filters (PSA-spectra, Eq. (8)) that bandpass  $\exp(i\varphi_1)$  and  $\exp(i\varphi_1)$  from 5 phase-shifted interferograms (Eq. (6)) as,

$$\begin{aligned}
H_1(\omega) &= (1 - e^{i\omega}) [1 - e^{i(\omega+\omega_2)}] [1 - e^{i(\omega-\omega_2)}] [1 - e^{i(\omega+\omega_1)}], \\
H_2(\omega) &= (1 - e^{i\omega}) [1 - e^{i(\omega-\omega_1)}] [1 - e^{i(\omega+\omega_1)}] [1 - e^{i(\omega+\omega_2)}].
\end{aligned} \tag{31}$$

- b) We then jointly optimize  $\{H_1(\omega), H_2(\omega)\}$  for high signal-to-noise ratio  $G_{S/N}(d)$  (Fig. 7) and obtained the PZT-step  $d$  at which that local maximum occurs.
- c) Having an optimum PZT-step  $d$ , we then calculate the tuning frequencies  $\omega_1 = (2\pi / \lambda_1)d$ ,  $\omega_2 = (2\pi / \lambda_2)d$ , which substituted back into  $\{H_1(\omega), H_2(\omega)\}$  give the specific DW-PSAs that phase-demodulate  $\varphi_1(x, y)$  and  $\varphi_2(x, y)$  (Eqs. (11-12)).
- d) We then plot (Fig. 8) the  $S/N$ -optimized designs  $\{H_1(\omega), H_2(\omega)\}$  to gauge their spectral behavior within  $\omega \in [-\pi, \pi]$  (Fig. 8).
- e) We also plotted (Fig. 14) the  $S/N$ -optimized  $\{H_1(\omega), H_2(\omega)\}$  designs for an extended frequency range of  $\omega \in [-30\pi, 30\pi]$ , to gauge their harmonic-rejection.
- f) With the  $S/N$ -optimized  $\{H_1(\omega), H_2(\omega)\}$  designs we quantified the harmonic-rejection capacity for each DW-PSA (Eq. (23)).
- g) For poor PZT-calibration we modified  $\{H_1(\omega), H_2(\omega)\}$  by raising the first-order zeroes to second-order zeroes, *i.e.*  $(\omega - \omega_1) \Rightarrow (\omega - \omega_1)^2$ ,  $(\omega - \omega_2) \Rightarrow (\omega - \omega_2)^2$ , etc.; making  $\{H_1(\omega), H_2(\omega)\}$  robust to detuning at the rejected frequencies (Fig. 13).
- h) We used the  $S/N$ -optimized designs to phase-demodulate 5 phase-shifted interferograms (Figs. 9-10) with high signal-to-noise and no phase cross-talking.
- i) Finally we extended the DW-PSA theory to 3-wavelengths  $\{\lambda_1, \lambda_2, \lambda_3\}$ ; further  $K$ -wavelengths  $\{\lambda_1, \lambda_2, \dots, \lambda_K\}$  generalization of this theory is just a matter of mathematical induction.

Finally, two examples of DW-PSA demodulation with  $\{\lambda_1 = 632.8\text{nm}, \lambda_2 = 532\text{nm}\}$  which illustrate the behavior of the synthesized PSAs were given. As far as we know, previous art on DW-PSAs [2-5, 14-19] only provided *ad-hoc* multi-wavelength PSA designs. Thus, this is the

first time that a general theory for synthesizing and analyzing multi-wavelength temporal phase-shifting algorithms is presented, and from which one may derive quantifying formulas for: (a) the PSAs spectra for each wavelength, (b) the PSAs signal-to-noise robustness for each wavelength, (c) the PSAs detuning sensitivity, and (d) the PSAs harmonics rejection for each wavelength.

### **Acknowledgments**

The authors acknowledge the financial support of the Mexican National Council for Science and Technology (CONACYT), grant 157044. Also the authors acknowledge Cornell University for supporting the e-print repository arXiv.org and the Optical Society of America for permitting OSA's contributors to post their manuscript at arXiv.